Journal of
Materials Chemistry A

Accepted Manuscript

Enhanced photocatalytic H_2 evolution on ZnS loaded with graphene and MoS_2 nanosheets as cocatalysts

Bolin Zhu, Bizhou Lin*, Yi Zhou, Ping Sun, Qianru Yao, Yilin Chen and Bifen Gao

---

Fujian Key Laboratory of Functional Materials, College of Materials Science and Engineering, Huaqiao University, Xiamen 361021, P. R. China. E-mail address: bzlinhqu@126.com; Fax: +86-592-6162221.

ABSTRACT

Graphene and MoS_2 nanosheets modified ZnS nanoparticles was successfully prepared by a simple one-pot hydrothermal route in the presence of graphene and MoS_2 nanosheets. The resultant ZnS/graphene/MoS_2 nanocomposites exhibited significantly enhanced photocatalytic activity and good recurrence stability in H_2 evolution from water splitting. When the loading content of graphene was 0.25 wt% and that of MoS_2 was 2 atom%, the ZnS/graphene/MoS_2 nanocomposite reached a high H_2-evolution rate of 2258 $\mu mol \cdot h^{-1} \cdot g^{-1}$ under a 300-W Xe lamp irradiation, which is about 2 times that of ZnS alone. The synergistic effect of cocatalysts contribute to the high performance of the hybrid photocatalyst, where graphene serves as an excellent electron acceptor and transporter, and MoS_2 nanosheets provides a source of active reactive sites. It demonstrates that the exfoliated MoS_2 nanosheets, achieved by the liquid exfoliation from natural molybdenite, can be used as one of efficient cocatalysts to prepare high-performance photocatalysts in hydrogen evolution from water splitting.

1. Introduction

The global energy crisis and the environmental pollution are two principal issues for human being due to fossil fuel combustion. Hydrogen, a clean energy, has been the generally accepted energy substitute for the fossil fuels.[1–4] However, hydrogen production through electrolysis or from fossil fuels is not environmental and not economical. Since Fujishima and Honda reported the photoelectrochemical water-splitting on the TiO_2 electrode in 1972,[5] photocatalytic H_2-production from water using semiconductor photocatalysts has attracted extensive attention.[2,3,6–9] The effective conversion of solar energy is of great importance for achieving an environmental friendly society. Among the investigated photocatalysts, mental sulfides have been widely studied due to their suitable bandgaps and photocatalytic performances.[10–14] ZnS is one of the most studied photocatalysts with a highly negative

reduction potential of excited electrons and a rapid generation of electron-hole pairs under light irradiation.[12–14] However, the rapid recombination of electron-hole pairs limited its practical applications.

In order to suppress the rapid recombination of electron-hole pairs for improving the photocatalytic H_2-production performance, cocatalysts are always introduced in photocatalysts.[3,15] Graphene, a single layer of graphite, possesses an extremely high specific surface area and an excellent electron transport property.[16,17] Numerous of efforts have been made to combine graphene with semiconductors for enhancing their photocatalytic performance.[16–21] For instance, Peng and coworkers reported that CdS exhibited a high photocatalytic H_2-production activity by combining with graphene, in which the coupled graphene cocatalyst serves as the electron acceptor to inhibit recombination of photogenerated charge carriers.[18,20] On the other hand, molybdenum disulfide (MoS_2) with a two-dimensional structure also has been proven as a promising cocatalyst for H_2 evolution.[22–25] Nanosized MoS_2 with a quantum-confinement effect exhibits the capacity of good reduction for protons, and MoS_2 nanosheet edges can promote the decomposition of water, which leads to efficient photocatalytic reactions. Li and coworkers demonstrated that CdS loaded with 0.2 wt% MoS_2 achieved a higher activity than CdS loaded with 0.2 wt% Pt, indicating that MoS_2 can be used as an effective cocatalyst to replace expensive Pt and other noble metals.[22] Very recently, Yu and coworkers reported that TiO_2 grown on layered graphene/MoS_2 hybrid showed a high photocatalytic activity towards H_2 generation.[15] In theses works, MoS_2 was synthesized from $(NH_4)_2MoS_4$ or Na_2MoO_4 as its precursors and presented in the form of several sheets. It is known that the individually single-layer MoS_2 nanosheets with a high specific surface area can be achieved through exfoliating natural molybdenite,[26,27] which offers a facile and economical approach to prepare MoS_2 nanosheets. However, it is surprising that there is no report using the exfoliated MoS_2 nanosheets as the cocatalyst to combine with semiconductor

photocatalysts up to date. Herein we report for the first time the preparation of ZnS nanoparticles through a simple one-pot hydrothermal method in the presence of graphene and MoS_2 nanosheets. The nanosheets of graphene and MoS_2 were served as the platforms for immobilizing ZnS nanoparticles. Due to the synergistic effect between the components, the resultant ZnS/graphene/MoS_2 nanocomposites exhibited significantly enhanced photocatalytic activities and good stability in H_2 evolution from water splitting. This study demonstrates that the exfoliated MoS_2 nanosheets can be used as one of efficient cocatalysts to prepare high-performance photocatalysts in hydrogen evolution from water splitting.

2. Experimental

2.1 Preparation of photocatalysts

All the reagents were of analytical-grade and were used as received without further purification. Graphene oxide (GO) was prepared by a modified Hummers' method from natural graphite powder.[28] Typically, a 9:1 mixture of concentrated H_2SO_4/H_3PO_4 (130:14 mL) was added to the mixture of graphite powder (1.0 g) and $KMnO_4$ (6.0 g) and then heated to 50°C with stirring for 12 h. The mixture was subsequently cooled to room temperature and poured onto ice (~250 mL) with 30% H_2O_2 (2 mL). The resultant mixture was centrifuged (9000 rpm for 15 min) and washed for several times with distilled water, 30% HCl and ethanol. The remaining solid was then dispersed with distilled water (200 mL) under ultrasonication at room temperature for 30 min to obtain the exfoliated GO nanosheets. A small amount of incompletely exfoliated particles was removed away using a centrifugation at 300 rpm for 10 min.

The exfoliated MoS_2 nanosheets were synthesized by a solvothermal method.[27] Firstly, 0.5 g MoS_2 and 0.5 M *n*-butylithium (15 mL) were added to *n*-hexane (35mL) in a 100 mL Teflon-lined stainless steel autoclave and heated at 100°C for 5 h. The product (Li_xMoS_2) was

rinsed three times with *n*-hexane and dried in vacuum at 50°C for 10 h. Secondly, 0.1 g Li_xMoS_2 was hydrolysed in 200 ml water (pH = 4, adjust with HNO_3) under ultrasonication for 60 min at room temperature to produce a colloidal suspension of MoS_2 nanosheets.

The ZnS/graphene/MoS_2 composites were synthesized by a hydrothermal method. $Zn(Ac)_2{\cdot}2H_2O$ and Na_2S were used as the precursors of ZnS. Firstly, 0.3 g sodium dodecylsulfate (SDS) was added to the distilled water (25 mL) to form a solution. Prior to the addition of GO suspension and MoS_2 nanosheets suspension, 0.88 g $Zn(Ac)_2{\cdot}2H_2O$ was dissolved in the SDS solution. Subsequently, Na_2S (0.2 M, 20 mL) was added dropwise to the mixture with stirring for 60 min and then transferred into a Teflon-lined autoclave and heated at 160°C for 2 h. The precipitates were collected and washed thoroughly with distilled water and ethanol for three times. Finally, the resultant products were dried at 60°C in vacuum over night. As discussed later, partial graphene oxide were reduced under the hydrothermal conditions, and are referred as RGO (shortened for reduced graphene oxide). By varying the addition amount, ZnS/graphene/MoS_2 nanocomposites with different RGO and MoS_2 amount were prepared. Hereinafter, ZnS with RGO (wt %) alone and MoS_2 nanosheets (atom% of metal elements) alone were respectively denoted as ZG*x* (*x* = 0.1, 0.25, 0.5, 1.0) and ZM*x* (*x* = 0.5, 1, 2, 4), and ZnS with 0.25% GO (wt%) and MoS_2 (atom%) was referred as ZGM*x* (*x* = 1.0, 2.0, 4.0).

2.2 Characterization

Powder X-ray diffraction (XRD) patterns were collected at room temperature on a Rigaku SmartLab 3KW diffractometer using Cu Kα radiation (λ = 0.15405 nm). Field emission scanning electron microscope (SEM) images were observed with a Hitachi S-4800 microscope, equipped with an Oxford 7021 spectrometer to examine energy dispersive X-ray spectroscopy (EDS). High-resolution transmission electron microscope (HRTEM) images

were taken using a JEOL JEM-2100 with an accelerating voltage of 300 kV. The samples were suspended in ethanol and sonicated over 10 min. Subsequently, a drop of the supernatant dispersion was placed onto a carbon film supported by a copper grid. UV-vis diffuse reflectance spectra were recorded on a Shimadzu UV-2550 spectrophotometer equipped with a 60-mm integrating sphere using $BaSO_4$ as the reference. The Kubelka-Munk function is defined as $F(R) = (1 - R)^2/2R$. Raman spectra were recorded using a micro-Raman spectrometer (Renishaw InVia) in the backscattering geometry with a 514.5 nm Ar^+ laser as an excitation source. Specific surface area and porosity measurements were carried out on a Nova 1200e instrument at liquid-nitrogen temperature using ultrapure nitrogen gas as the adsorbate, in which all samples were degassed at 200°C for 4 h in flowing N_2 prior to the measurements. X-ray photoelectron spectroscopy (XPS) measurements were performed on a VG Escalab MK II spectrometer (Scientific Ltd.) with nonmonochromatic Al K X-ray (1486.6 eV). The pressure in the chamber during the experiments was less than 10^{-6} Pa. The analyzer was operated at 20 eV pass energy with an energy step size of 0.1 eV. Infrared spectra were recorded at room temperature on a Nicolet 470 FT-IR spectrophotometer as KBr pellets in the 4000–400 cm^{-1} region.

2.3 Photoelectrochemical measurements

Photoelectrochemical behaviors were carried out in a three-electrode quartz glass cell using a CHI660B potentiostat/galvanostat (Chenhua instruments, Shanghai), where a Pt wire and Ag/AgCl electrode (saturated KCl) were used as the counter and reference electrodes, respectively. The working electrode was prepared as follows. 0.1 g sample was dispersed in distilled water (5 mL) and sonicated for 30 min to make slurry. The slurry was then coated onto an indium-tin oxide-coated glass with an active area of ca. 0.75 cm^2. After that, the electrode was dried in vacuum at 60°C. A propylene carbonate solution containing 0.1 M

$LiClO_4$ was used as the supporting electrolyte. The monochromatic light of 340 nm was employed as the excitation light source with an incident intensity of 60 μW/cm^2, obtained from a Zolix Omni-λ150 grating monochromator with a 300 W Xenon lamp, to explore the light responses.

2.4 Photocatalytic test

The photocatalytic H_2 evolution performance was carried out on a CEL-SPH2N photocatalytic water-splitting system (Aulight Tech Co. Ltd, Beijing), with a top-irradiation 500-mL Pyrex vessel. A 300 W xenon lamp was used as the irradiation (1 cm far away from the quartz cap) with an incident intensity of 125 mW/cm^2. 100 mg photocatalyst was dispersed with a constant stirring in a 100 mL aqueous solution containing 0.005 M Na_2S and 0.005 M Na_2SO_3 as the sacrificial reagents. Prior to irradiation, the reactor was sealed and then thoroughly degassed to completely remove air and to ensure the reaction system under anaerobic conditions. A continuous magnetic stirrer was applied at the bottom of the reactor in order to keep the photocatalyst particles in suspension status during the whole experiments. The evolved hydrogen amount was measured by an online gas chromatograph (Shimadzu GC7890II, thermal conductivity detector, 5Å molecular sieve columns and Ar carrier).

3. Results and discussion

3.1 Structural and morphological analyses

As shown in Fig. 1, three pronounced peaks at 28.6° (111), 47.5° (220) and 56.3° (311) in all samples can be indexed to those of the cubic sphalerite ZnS (JCPDS no 05-0566). The broad diffraction peaks of ZnS are due to its small crystallite size. However, the peaks of ZG0.25 have become narrower significantly, and a small peak appears at 33.1° is observed, which can be ascribed to the (002) facet of cubic ZnS. The narrower peaks indicate that the average

crystallite size of ZnS in ZG is bigger than that of the bare ZnS, demonstrating that a certain amount of graphene may promote the growth and aggregation of ZnS nanoparticles (Fig. S1 in the Supplementary Information). However, in the presence of MoS_2 nanosheets and in the coexistence of graphene and MoS_2 nanosheets under the hydrothermal preparation conditions, all of the obtained ZM and ZGM composites exhibited broad diffraction peaks, similar to the bare ZnS. Such broadening is enough to shield the (002) reflection, similar to the previous reports.[29] The broad diffraction peaks suggest that the presence of MoS_2 nanosheets prevented the crystallite growth of ZnS. The small crystallite size is favorable for the improvement in surface area. The average crystallite sizes of ZnS particles for typical samples are listed in Table 1, calculated from the 28.6° peak by the Scherrer's formula. It should be pointed out that no apparent peaks for graphene or MoS_2 were observed because of their lower loading content and weak crystallization. However, their existence can be clearly identified by HRTEM, XPS and Raman spectra as discussed later.

TEM and HRTEM images were taken to directly analyze the microscopic morphology and structural information of ZGM composites. As documented in Fig. 2, although some graphene are curly, most of them are functioned as the supported platform for the deposition of exfoliated MoS_2 nanosheets and the growth of the ZnS nanoparticles. The compositions in ZGM2, ZnS, graphene and MoS_2, have been integrated by the way of intimated interfacial contact. It was supported by FT-IR spectra (Fig. S2), where the featured 659 cm^{-1} of Zn–S stretch for ZnS was shifted to 664 cm^{-1} and 615 cm^{-1} of Mo–S stretch for MoS_2 to 620 cm^{-1} in ZGM2. The intimated contact is expected to form a desirable heterostructure, which will lead to more efficient electron transfer between the adjacent components. The lattice fringes presented in different directions can be clearly observed in a same area (Fig. 2C). The lattice spacing of about 0.31 nm can be ascribed to the (111) plane of cubic ZnS, and the spacing of about 0.27 nm to the (100) plane of hexagonal MoS_2. The latter demonstrates the atomic

lattices in the MoS_2 basal planes, suggesting that the MoS_2 sheets lay flat on the graphene. The content of MoS_2 in ZGM2 determined by EDS (Fig. S3) was 2.18 atom%, which is in good agreement with the addition amount. As depicted in Fig. 2C, each agglomerated ZnS nanoparticle presents almost the same size, indicating the growth of ZnS nanoparticles may be possible upon Ostwald ripening.[29] The mechanism is responsible for the nucleation of ZnS small particles as well as the dissolution of small crystals which are deposited onto larger crystals, which results in the uniform size under the employed conditions.

3.2 XPS spectra

The XPS spectra of C 1s S 2p, Zn 2p and Mo 3d in materials are plotted in Fig. 3, and the corresponding binding energies are listed in Tables 2 and 3. The C 1s profile of GO can be analyzed into three peaks, which corresponds to carbon atoms in different functional groups (Fig. 3A). The peak at 284.6 eV can be assigned to the sp^2 bonded carbon present in graphitic domains, that at 286.6 eV to the C–OH group and that at 287.3 eV to the carbonyl C=O group, respectively.[28,30] In contrast to GO, the O-related peaks of ZGM2 show a notable decrease (Fig. 3B). The peak corresponding to the C=O group vanished away, and a lower peak at 288.5 eV, ascribed to the C–O group, was found. Moreover, its C–OH peak at 286.6 eV is weaker than that of GO. The observations provide strong evidences for the reduction of GO species during the formation of ZGM2 composites under the hydrothermal conditions. The results are further supported by Raman spectra. The C–O and C–OH surface functional groups provided active sites for the directed deposition of ZnS nanocrystals on the surface of graphene.

The data of Zn 2p in ZnS, 1044.1 and 1022.1 eV, are in consistent with the reported values of ZnS.[31,32] As plotted in Fig. 3D, the peaks emerge a slightly positive shift with the addition of GO and MoS_2. Due to the large amount of electron-attracting groups, the electrons around

Zn^{2+} transfer to the surface of RGO and/or MoS_2, which decreases the electron density and results in the increase of binding energies of Zn. The spectra of S 2p and Mo 3d are displayed in Figs. 3C and 3E. The shifts of binding energy in ZGM2 indicate the presence of the electron coupling among ZnS, RGO and MoS_2, which will be beneficial to the efficient charge transfer between the adjacent components during the photocatalytic reaction.

3.3 Raman spectra

Two typical peaks of graphene can be easily observed in Raman spectra (Fig. 4). The D-band at 1354 cm^{-1} evolved from the structural imperfections is created by the sp^3 C atom from the oxygen-containing functional groups, whereas the G-band occurred at 1595 cm^{-1} can be assigned to the sp^2 C atom on the graphene basal plane.[28,33,34] The intensity ratio of D-band to G-band (I_D/I_G) is a measurement of the defects in graphene.[28] Compared with GO (I_D/I_G = 0.89), ZG0.25 and ZGM2 displayed a slight decrease in I_D/I_G (both are 0.84). It is regarded as the decrease of sp^3 C atom, indicating the removal of oxygen-containing functional groups like hydroxyl and epoxy to some extent. The reduction of graphene will improve the mobility of the electrons, which results in the efficient enhancement of photocatalytic process. In addition, two Raman active modes can be identified obviously at 383 and 409 cm^{-1}, which can be ascribed to the E^1_{2g} and A_{1g} modes of MoS_2.[35]

3.4 Nitrogen adsorption–desorption isotherms

Heterogeneous photocatalysis is a surface-controllable process, and a large surface area contributes to the enhancement of photocatalytic activity due to more surface active sites for the adsorption of reactant molecules.[3,36,37] Fig. 5 presents the N_2 adsorption–desorption isotherms and the corresponding pore size distribution curves of ZnS, ZG0.25, ZM2 and ZGM2. The isotherms can be assigned as type IV according to the BDDT classification,

indicating the presence of mesopores.[38,39] However, these isotherms show different hysteresis loops. ZnS, ZM2 and ZGM2 show distinct hysteresis loops of type H4 in the p/p_0 range of 0.4~0.9, indicating the presence of mesopores.[11,38] And ZG0.25 shows an H3 hysteresis loop in the p/p_0 range of 0.7~1.0 with no saturated adsorption till p/p_0 = 1.0, suggesting the formation of large mesopores.[38,39] The pore size distributions (inset in Fig. 5) of the samples indicate a wide pore-size distribution from 2 to 15 nm, further confirming the presence of mesopores. The BET specific surface areas, calculated from the desorption portion with the p/p_0 under 0.3, were determined to be 124, 94, 178 and 149 $m^2 \cdot g^{-1}$ for ZnS, ZG0.25, ZM2 and ZMG2, respectively (Table 1). As mentioned above, the concentrations of graphene and MoS_2 in the composites are low, it is expected that the additions have no evident influence on the surface areas of the samples. However, it is reasonable to expect that the change of specific surface area is relative with the multiarchitecture in composites containing ZnS, graphene and MoS_2. The reduction of ZG0.25, compared to that of the bare ZnS, may be ascribed to the fact that GO can promote the growth and aggregation of ZnS nanoparticles due to the abundant surface groups of GO. The increase of ZMG2 may be originated from the fact that the MoS_2 sheets shielded part of GO, which prevented the ZnS nanoparticles from aggregation. The results of surface areas are in accordance with the expectation of XRD analyses.

3.5 UV-Vis diffuse reflectance spectra

Fig. 6 shows the comparison of the UV-vis diffused reflectance spectra of ZnS, ZG0.25, ZM2 and ZGM2. The obvious decrease in the absorption at wavelengths range up to 370 nm can be ascribed to the intrinsic bandgap absorption of ZnS, and its corresponding bandgap energy is estimated to be 3.35 eV, consistent with the reported value.[13] With the addition of small amount of graphene and MoS_2, a slightly red-shift was clearly observed. The absorption edges of ZG0.25, ZM2 and ZGM2 are shifted to 381, 378 and 383 nm with the corresponding

bandgaps of 3.26, 3.28 and 3.24 eV, respectively. Such small shifts provide an indicator that the nanosheets of graphene and MoS_2 only provide the supports for immobilizing ZnS nanoparticles. And these small shifts are just resulted from the heterostructure within their intimated interfacial contact. In addition, the ZG0.25, ZM2 and ZGM2 composite samples extend their broad background absorption in the visible-light region, which can be ascribed to the presence of graphene and MoS_2.

3.6 Photoelectrochemical properties

The transient photocurrent responses without applied bias potential are presented in Fig. 7. All the samples showed a negative photocurrent response, the characteristic of p-type semiconductors.[40] ZnS displayed an obvious photocurrent boost as soon as the light turned on, indicating a number of electrons were generated. The photocurrent was gradually reduced in the following 20 s, which can be contributed to the recombination of photogenerated electron-hole pairs, similar to the observation by Yu.[32] In contrast, the photocurrent of ZG0.25 containing graphene showed a slow growth process when the light turned on. This is because that the graphene has a lower Femi level than the conduction band of ZnS,[41] a large number of electrons transfer to the graphene and only a part of electrons can be detected, causing a slow response in photocurrent. The curves would not reach equilibrium until the graphene saturated with electrons. Similarly, when the light was switched off, the photocurrent delayed to the baseline with a slow response because of the electrons release from the graphene. It implies that graphene takes a role of an electron collector and transporter for effectively suppressing the charge recombination, leading to leaving more charge carriers to form reactive species, which in turn results in a high photocurrent response and an improved photocatalytic activity.[32] ZM2 exhibited a moderate photocurrent, higher than ZnS and lower than ZG0.25, and a responsive behavior similar to ZG0.25. It implies that the excited electrons of ZnS can

transfer to MoS_2 nanosheets, which can inhibit the recombination of photogenerated charge carriers in some extent. Compared with ZG0.25 and ZM2, ZGM2 showed a relative strong photocurrent response. It further suggests that MoS_2 is also an excellent electron-acceptor in such a composite system, which further improves the separation efficiency of photogenerated electron-hole pairs, efficiently reduces their recombination possibility and ultimately enhances the production of photocurrent. A strong photocurrent response is expected to exhibit relative higher photocatalytic activities in the photocatalytic hydrogen evolution. This observation indicates that MoS_2 can be used as one of promising cocatalysts, substitute for the noble metals, in photocatalysts. In addition, a relative weak photocurrent response of graphene and MoS_2 hybrid (MG, prepared under the same conditions as ZGM2 but without ZnS) was also shown in the Fig. 7.

3.7 Photocatalytic activities

The photocatalytic activities of the investigated samples were evaluated by measuring H_2 production from water splitting in a Na_2S/Na_2SO_3 aqueous solution. The rates of H_2 evolution in the presence of different catalysts are presented in Fig. 8, showing the average results of 3 repeating experiments with an error bar for each case. The bare ZnS without graphene and MoS_2 showed a rate of 1185 $\mu mol \cdot h^{-1} \cdot g^{-1}$. It was noted that the only trace hydrogen was detected when the RGO alone was employed as a photocatalyst, and the H_2 evolution rates of MoS_2 alone and MG hybrid were very low (47 and 96 $\mu mol \cdot h^{-1} \cdot g^{-1}$, respectively) under the same experimental conditions. This indicates that ZnS is the predominating active component for photocatalytic H_2 evolution in the nanocomposites. With increasing RGO content, the photocatalytic activities of ZG increased initially and then decreased. With a small amount of graphene under 0.25%, the H_2 evolution rates of ZG0.1 and ZG0.25 were greatly enhanced to achieve 1277 and 1688 $\mu mol \cdot h^{-1} \cdot g^{-1}$, respectively. However, the rate showed a decrease with

the amount of RGO over 0.5%, and only 1129 and 724 μmol·h^{-1}·g^{-1} for ZG0.5 and ZG1.0 were observed, respectively. This variation tendency is similar to the previous reports for the CNT-$Zn_{0.9}Cd_{0.1}S$ and RGO-$Zn_{0.8}Cd_{0.2}S$ systems.[12,32] When the optimized RGO content was fixed at 0.25% and the addition amount of MoS_2 sheet was varied from 1% to 4%, the relationship between the H_2 evolution rate and the MoS_2 content of the resultant ZGM composites exhibited a similar variation tendency to that of ZG with the varied RGO content. After adding 1 and 4 wt % of MoS_2, the rates of H_2 evolution on ZGM1 and ZGM4 were 1883 and 1825 μmol·h^{-1}·g^{-1}, respectively, both of them showed lower photocatalytic activities than ZGM2 containing 2% MoS_2. The ZGM2 showed the highest H_2 evolution among all the samples and achieved at a rate of 2258 μmol·h^{-1}·g^{-1}. Why the photocatalytic activities decreased when the addition of RGO and MoS_2 exceeded a certain amount? This probably is due to the following factors: (i) with the amount of RGO and MoS_2 increases, the color of samples becomes darker and darker, ranging from white to grey and then light dark. The introduction of a large percent of black components shielded the incident light from irradiating into the inside of ZG, and ZGM nanocomposites, which has been encountered in the previous studies;[12,15,23,32] (ii) the excessive RGO and MoS_2 sheets may cover the active sites on the surface of ZnS and hinder the contact of the sacrificial agents with the active ZnS. Hence, it is of great importance for optimizing the photocatalytic activities of photocatalyst with suitable dosages of RGO and MoS_2.

As mentioned above, in the as-prepared nanocomposites, ZnS is the predominating active component for photocatalytic H_2 evolution, and RGO is an electron collector and transporter. The interfacial interaction between ZnS and RGO favors the vectorial transfer of the photogenerated electrons from the conduction band (CB) of ZnS to RGO. This space separation of the photogenerated electrons and holes is beneficial for preventing the charge recombination, which in turn results in a high photocatalytic activity.[42] A schematic

representation for the photocatalytic mechanism is depicted in Fig. 9. Under the irradiation of a 300W Xe lamp, electrons in the valence band (VB) of ZnS (2.36 V vs SHE) are excited to CB (–1.04 V vs SHE), leaving a hole in VB. Normally, these photogenerated charge carriers recombine rapidly and only a fraction of electrons and holes transfer to the surface of the photocatalyst to reduce H^+ to H_2, conducing a low photocatalytic activity. However, when ZnS nanoparticles are immobilized on the surface of RGO, the CB electrons of ZnS tend to migrate quickly to RGO, which possesses a high electrical conductivity and a relatively lower redox-potential position (–0.08 V vs SHE).[43] The mobility of these electrons on the graphene sheets is extremely high. RGO can function as an excellent electron acceptor and transporter to efficiently prolong the lifetime of charge carriers and consequently improve the charge separation efficiency and the catalytic H_2 evolution activity of ZG composites.

The MoS_2 sheets in ZGM composites can accept electrons since the CB potential of MoS_2 (0.20 V vs SHE)[44] is more positive than that of RGO. Nanosized MoS_2 is a good catalyst for the reduction of protons as a result of the quantum-confinement effect, and the edges of MoS_2 sheets can promote the dissociation of water and the production of H_2.[15,45–49] In other words, the photogenerated CB electrons of ZnS can be transferred to the MoS_2 nanosheets through RGO (serving as a role of the conductive electron transporter) and then react with the adsorbed H^+ ions at the edges of MoS_2 to form H_2. MoS_2 nanosheets are expected to provide abundant exposed active sites, thus leading to an enhancement in photocatalytic activity for H_2 evolution. The synergistic effect between RGO, MoS_2 nanosheets and ZnS will further inhibit the charge recombination, improve the interfacial charge transfer, and consequently enhance the photocatalytic activities of ZGM composites. On the other hand, some photogenerated CB electrons of ZnS can also be transferred directly to MoS_2 nanosheets on the surface of ZnS to react with the absorbed H^+ to produce H_2. As seen from Fig. S4, under the same reactant conditions, ZM composites containing MoS_2 sheet ranging from 0.5 to 4

wt % and without RGO exhibited H_2 evolution rates from 1282 to 1605 μmol·h^{-1}·g^{-1}, which are greater than that of ZnS alone (1185 μmol·h^{-1}·g^{-1}). After using MoS_2 and RGO as cocatalysts, the photocatalytic activities of ZGM composites are further improved, as mentioned above. A comparative experiment using a physical mixture of ZnS, RGO and MoS_2 with the same content as ZGM2 as the photocatalyst was carried out. It got a rate of 1252 μmol·h^{-1}·g^{-1}, much lower than that of ZGM2 (2258 μmol·h^{-1}·g^{-1}). It demonstrates that the synergistic effect between RGO, MoS_2 nanosheets and ZnS plays a crucial role in the hydrogen evolution. The aforementioned three ways, in which photogenerated electrons in CB of ZnS are transferred, effectively improve the spatial separation of the photogenerated electron−hole pairs, greatly enlarge the reaction space, and ultimately enhance the photocatalytic activity.

Metal sulfides always show declination in their photocatalytic activities because of photocorrosion.[2,9,12] To verify the stability and recycling performance of the as-prepared nanocomposites, the time-dependences of the photocatalytic H_2 evolution over ZG0.25, ZM2 and ZGM2 from aqueous solutions containing Na_2S and Na_2SO_3 under a 300 W xenon lamp as the light irradiation were carried out. The reaction system was evacuated every 3 h. As shown in Fig. 10, there was no obvious activity drop after each run, indicating better stability and recycling performance of our samples, in which ZnS was loaded with RGO or/and MoS_2 as cocatalysts in hydrogen evolution.

Conclusions

This work demonstrates a facile way to successfully prepare ZnS loaded with graphene and MoS_2 nanosheets as cocatalysts by a simple hydrothermal method. The photocatalytic rate of H_2 evolution on ZnS was improved by loading graphene and MoS_2 nanosheets as cocatalysts. The optimal loading contents were determined to be graphene 0.25 wt% and MoS_2 2 atom%

and the corresponding H_2-evolution rate of 2258 μmol·h^{-1}·g^{-1}, which is about 2 times than that of ZnS alone. The resultant ZnS/graphene/MoS_2 nanocomposites also exhibited good stability and recycling performance. It has been revealed that both of graphene and MoS_2 nanosheets can be used as efficient cocatalysts as substitutes for noble metals in hydrogen evolution from water splitting. Notably, it is the first time to use the exfoliated MoS_2 nanosheets as the cocatalyst to hybridize with a photocatalyst. The exfoliated MoS_2 nanosheets can be achieved by the liquid exfoliation from natural molybdenite, which provides a feasible and economical approach for the design and preparation of high-performance photocatalysts.

Acknowledgments

This work was supported by the National Natural Science Foundation of China (50872037, 21003055, 21103054), and the Natural Science Foundation of Fujian Province (2010J01040).

References

1 J. Sato, N. Saito, Y. Yamada, K. Maeda, T. Takata, J. N. Kondo, M. Hara, H. Kobayashi, K. Domen and Y. Inoue, *J. Am. Chem. Soc*., 2005, **127**, 4150–4151.

2 X. B. Chen, S. H. Shen, L. J. Guo and S. S. Mao, *Chem. Rev*., 2010, **110**, 6503–6070.

3 X. Fan, B. Lin, H. Liu, L. He, Y. Chen and B. Gao, *Int. J. Hydrogen Energy*, 2013, **38**, 832–839.

4 X. Tang, Q. Tay, Z. Chen, Y. Chen, G. K. L. Goh and J. Xue, *J. Mater. Chem. A*, 2013, **1**, 6359–6365.

5 A. Fujishima and K. Honda. *Nature*, 1972, **238**, 37–38.

6 W. G. Wang, T. B. Rauchfuss. *J. Am. Chem. Soc*., 2012, **134**, 4525−4528.

7 L. Jia, D.H. Wang, Y. X. Huang, A.W. Xu, and H.Q. Yu. *J. Phys. Chem. C*, 2011, **115**, 11466–11473.

8 L. Ge and C. C. Han, *Appl. Catal. B: Environ*., 2012, **117**, 268–274.

9 J. Zhang, J. G. Yu, Y. M. Zhang, Q. Li and J. R. Gong, *Nano Lett*., 2011, **11**, 4774–4779.

10 Y. B. Wang, Y. S. Wang and R. Xu, *J. Phys. Chem. C*, 2013, **117**, 783–790.

11 J. G. Yu, B. Yang and B. Cheng, *Nanoscale*, 2012, 4, 2670–2677.

12 H. Fujiwara, H. Hosokawa, K. Murakoshi, Y. Wada and S. Yanagida, *Langmuir*, 1998, **14**, 5154–5159.

13 Y. H. Zhang, N. Zhang, Z. R. Tang and Y. J. Xu, *ACS Nano*, 2012, **6**, 9777–9789.

14 M. Luo, Y. Liu, J. C. Hu, J. L. Li, J Liu and R. M. Richards, *Appl. Catal. B: Environ*., 2012, **125**, 180–188.

15 Q. J. Xiang, J. G. Yu and M. Jaroniec, *J. Am. Chem. Soc*., 2012, **134**, 6575–6578.

16 V. Stengl, D. Popelkova and P. Vlacil, *J. Phys. Chem. C*, 2011, **115**, 25209–25218.

17 X. An, X. Yu, J. Yu and G. Zhang, *J. Mater. Chem. A*, 2013, **1**, 5158–5164.

18 T. Y. Peng, K. Li, P. Zeng, Q. G. Zhang and X. G. Zhang, *J. Phys. Chem. C*, 2011, **116**, 22720–22726.

19 Q. J. Xiang and J. G. Yu, *J. Phys. Chem. Lett.*, 2013, **4**, 753–759.

20 Q. J. Xiang, J. G. Yu and M. Jaroniec, *Chem. Soc. Rev*., 2012, **41**, 782–796.

21 Y. H. Zhang, Z. Chen, S. Q. Liua and Y. J. Xu, *Appl. Catal. B: Environ*., 2013, **140**, 598–607.

22 X. Zong, Y. Na, F. Y. Wen, G. J. Ma, J. H. Yang, D. G. Wang, Y. Ma, M. Wang, L. C. Sun and C. Li, *Chem. Commun*., 2009, 4536–4538.

23 X. Zong, H. J. Yan, G. P. Wu, G. J. Ma, F. Y. Wen, L. Wang and C. Li, *J. Am. Chem. Soc*., 2008, **130**, 7176–7177.

24 X. Zong, G. P. Wu, H. J. Yan, G. J. Ma, J. Y. Shi, F. Y. Wen, L. Wang and C. Li, *J. Phys. Chem. C*, 2010, **114**, 1963–1968.

25 Y. G. Li, H. L. Wang, L. M. Xie, Y. Y. Liang, G. S. Hong and H. J. Dai, *J. Am. Chem.*

Soc., 2011, **133**, 7296–7299.

26 V. Nicolosi, M. Chhowalla, M. G. Kanatzidis, M. S. Strano and J. N. Coleman, *Science*, 2013, **340**, 1226419.

27 B. Z. Lin, C. Ding, B. H. Xu, Z. J. Chen and Y. L. Chen, *Mater. Res. Bull*., 2009, **44** 719–723.

28 D. C. Marcano, D. V. Kosynkin, J. M. Berlin, A. Sinitskii, Z. Sun, A. Slesarev, L. B. Alemany, W. Lu and J. M. Tour, *ACS Nano*, 2010, **8**, 4806–4814.

29 S. K. Apte, S. N. Garaje, S. S. Arbuj, B. B. Kale, J. O. Baeg, U. P. Mulik, S. D. Naik, D. P. Amalnerkar and S. W. Gosavi, *J. Mater. Chem.*, 2011, **21**, 19241–19248.

30 H. J. Shin, K. K. Kim, A. Benayad, S. M. Yoon, H. K. Park, I. S. Jung, M. H. Jin, H. K. Jeong, J. M. Kim, J. Y. Choi and Y. H. Lee, *Adv. Funct. Mater*., 2009, **19**, 1987–1992.

31 J. F. Moulder, W. F. Sticke, P. E. Sobol and K. D. Bomben, *Handbook of X-Ray Photoelectron Spectroscopy*, Perkin-Elmer Corp, New York, 1992.

32 J. Zhang, J. G. Yu, M. Jaroniec and J. R. Gong, *Nano Lett*., 2012, **12**, 4584–4589.

33 J. X. Wang, P. X. Wang, Y. T. Cao, J. Chen, W. J. Li, Y. Shao, Y. Zheng and D. Z. Li, *Appl. Catal. B: Environ*., 2013, **136**, 94–102.

34 D. Graf, F. Molitor, K. Ensslin, C. Stampfer, A. Jungen, C. Hierold and L. Wirtz, *Nano Lett*., 2007, **7**, 238–242.

35 M. Shanmugam, C. A. Durcan and B. Yu, *Nanoscale*, 2012, **4**, 7399–7405.

36 J. G. Yu, L. J. Zhang, B. Cheng and Y. R. Su, *J. Phys. Chem. C*., 2007, **111**, 10582–10589.

37 R. M. Navarro, M. C. Alvarez-Galvan, J. A. V. de la Mano, S. M. Al-Zahrani and J. L. G. Fierro, *Energ. Environ. Sci*., 2010, **3**, 1865–1882

38 S. J. Gregg and K. S. Sing, *Adsorption, Surface Area and Porosity*, 2nd edn, Academic Press, Londn, 1983.

39 K. S. W. Sing, D. H. Everett, R. A. W. Haul, L. Moscou, R. A. Pierotti, J. Rouquerol, T.

Siemieniewska, *Pure Appl. Chem*., 1985, **57**, 603–1882.

40 Z. H. Zhang, R. B. Dua, L. B. Zhang, H. B. Zhu, H. N. Zhang and P. Wang, *ACS Nano* 2012, **7**, 1709–1717.

41 X. Wang, L. J. Zhi and K. Mullen, *Nano Lett*., 2008, **8**, 323−327.

42 J. Cao, J. Z. Sun, J. Hong, H. Y. Li, H. Z. Chen and M. Wang, *Adv. Mater.*, 2004, **16**, 84−87.

43 K. F. Zhou, Y. H. Zhu, X. L. Yang, X. Jiang and C. Z. Li, *New J. Chem*., 2011, **35**, 353−359.

44 L. F Schneerneyer and M. S. Wrighton, *J. Am. Chem. Soc*., 1979, **101**, 6496−6500.

45 Y. D. Hou, B. L. Abrams, Peter C.K. Vesborg, M. E. Björketun, K. Herbst, L. Bech. A. M. Setti, C. D. Damsgaard, T. Pedersen, O.Hansen, J. Rossmeisl, S. Dahl, J. K. Nørskov and I. Chorkendorff, *Nat. Mater*., 2011, **10**, 434−438.

46 Y. G. Li, H. L. Wang, L. M. Xie, Y. Y. Liang, G. S. Hong and H. J. Dai, *J. Am. Chem. Soc*., 2011, **133**, 7296−7299.

47 W. Zhou, Z. Yin , Y. Du, X. Huang, Z. Zeng, Z. Fan, H. Liu, J. Wang and H. Zhang, *Small*, 2013, **9**, 140–147.

48 J. G .Yu and J. R. Ran, *Energ. Environ. Sci*., 2011, **4**, 1364−1371.

49 N. Z. Bao, L. M. Shen, T. Takata and K. Domen, *Chem. Mater*., 2008, **20**, 110–117.

Table 1 Parameters obtained from XRD patterns and N_2 adsorption-desorption isotherms

Sample	Average crystallite size (nm) [a]	Specific surface area ($m^2 \cdot g^{-1}$) [b]	Average pore size (nm) [c]
ZnS	2.4	124	2.7
ZG0.25	14.1	94	5.9
ZM2	2.2	178	4.4
ZGM2	2.6	149	2.7

[a] average crystallite size was determined from the Scherrer's formula, $D = 0.9\lambda/\beta\cos\theta$.

[b] Specific surface area was calculated from the linear part of BET plot.

[c] Average pore diameter was estimated from the Barrett–Joyner–Halenda formula.

Table 2 Binding energies of C 1s and their corresponding functional groups

Sample	284.6 eV	286.6 eV	287.3 eV	288.5 eV
GO	C–C	C–OH	C=O	–
ZGM2	C–C	C–OH	–	C–O

Table 3 Binding energies (eV) obtained from XPS measurements

Sample	S $2p_{3/2}$	Zn $2p_{3/2}$	Zn $2p_{1/2}$	Mo $3d_{5/2}$	Mo $3d_{3/2}$
ZnS	161.6	1044.1	1022.1	–	–
ZG0.25	161.5	1044.5	1021.5	–	–
ZGM2	161.4	1044.6	1021.6	231.8	228.8
MoS_2	162.6	–	–	233.0	229.8

CAPTIONS TO FIGURES

Fig. 1. Powder XRD patterns of the as-prepared samples.

Fig. 2. Typical TEM (A and B) and HRTEM images (C) of ZGM2, where B is the detailed of the square frame in A and C is that in B.

Fig. 3. XPS spectra of C 1s (A and B), S 2p (C) and Zn 2p (D) in GO (a), ZnS (b), ZG0.25 (c) and ZGM2 (d), full spectrum of ZGM2 with magnified Mo 3d (E) and referred MoS_2 (F).

Fig. 4. Raman spectra of GO (a), ZG0.25 (b), ZGM2(c). The inset shows the detail of ZGM2 from 300 to 500 cm^{-1}.

Fig. 5. Nitrogen adsorption–desorption isotherms of ZnS, ZG0.25, ZM2 and ZGM2. The inset indicates their pore size distribution curves.

Fig. 6. UV-vis diffuse reflectance spectra of ZnS (a), ZG0.25 (b), ZM2 (c), ZGM2 (d) and RGO(e). The inset curve indicates the absorbance of MoS_2.

Fig. 7. Photocurrent-time curves of ZnS (a), ZG0.25 (b), ZM2 (c), ZGM2 (d) and MG (e).

Fig. 8. Comparison of the H_2-production rates on different catalysts under the employed conditions of 100 mg catalyst, 100 mL aqueous solution containing 0.005 M Na_2S and 0.005 M Na_2SO_3, and 300-W xenon lamp irradiation, where MIX for the physical mixture of ZnS, graphene and MoS_2.

Fig. 9. Proposed mechanism for the enhanced electron transfer in ZGM composites.

Fig. 10. Time-circle photocatalytic hydrogen evolution over ZG0.25 (a), ZM2 (b) and ZGM2 (c).

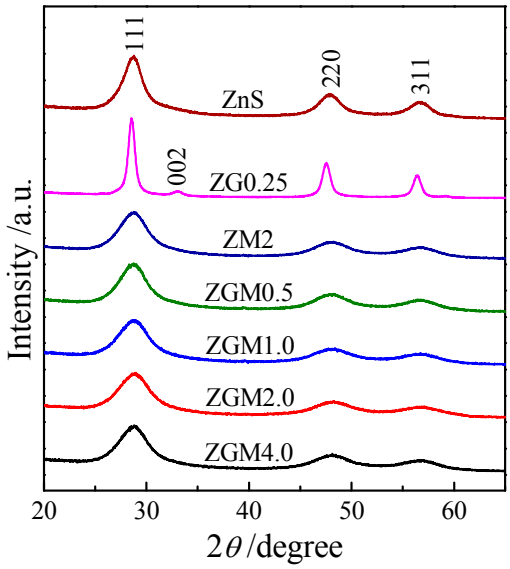

Fig. 1. Powder XRD patterns of the as-prepared samples.

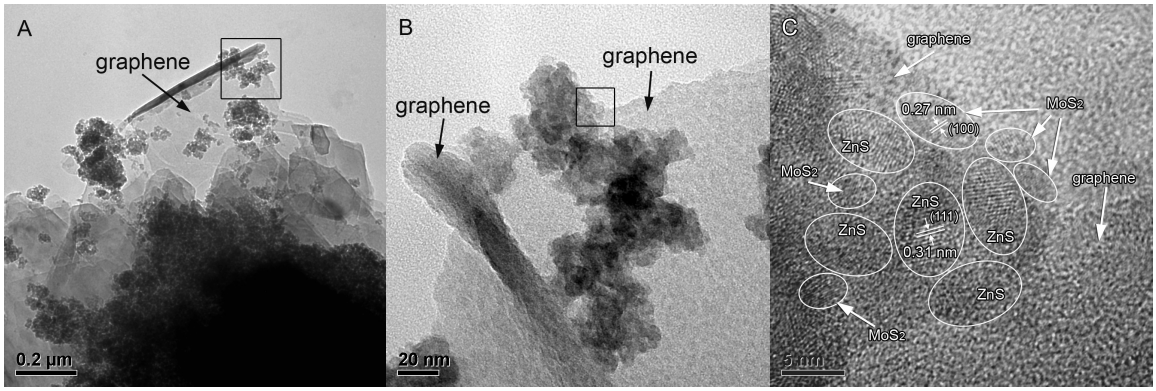

Fig. 2. Typical TEM (A and B) and HRTEM images (C) of ZGM2, where B is the detailed of the square frame in A and C is that in B.

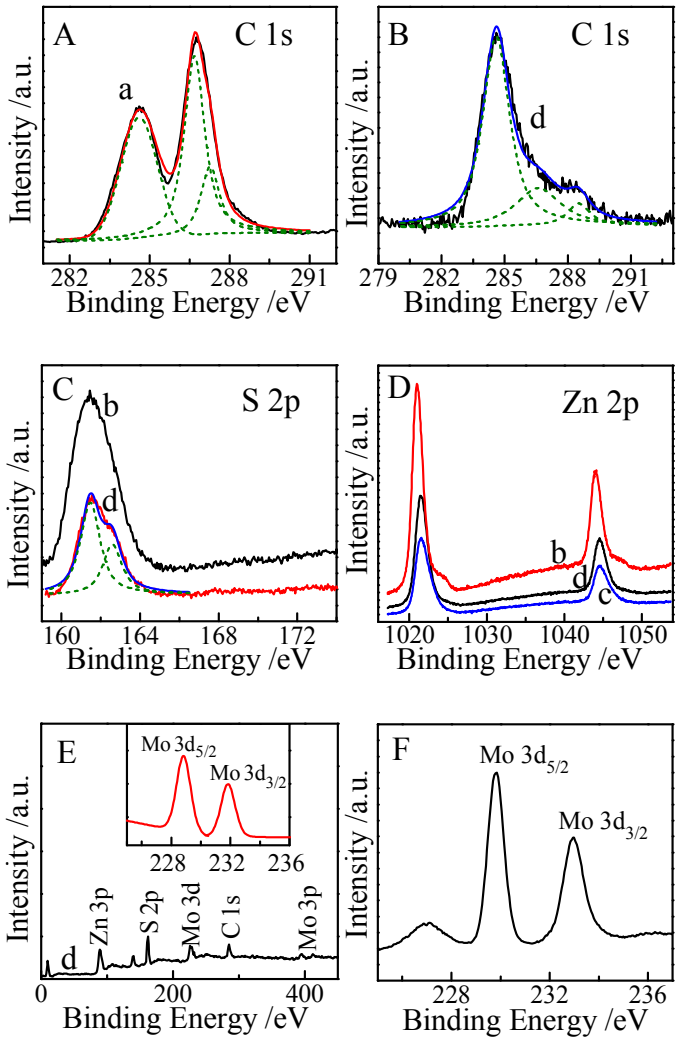

Fig. 3. XPS spectra of C 1s (A and B), S 2p (C) and Zn 2p (D) in GO (a), ZnS (b), ZG0.25 (c) and ZGM2 (d), full spectrum of ZGM2 with magnified Mo 3d (E) and referred MoS_2 (F).

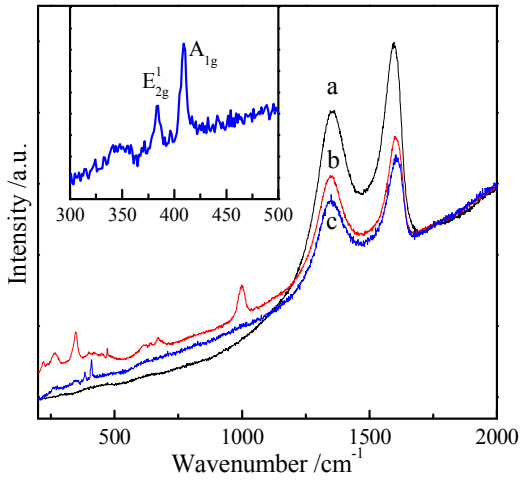

Fig. 4. Raman spectra of GO (a), ZG0.25 (b), ZGM2(c). The inset shows the detail of ZGM2 from 300 to 500 cm^{-1}.

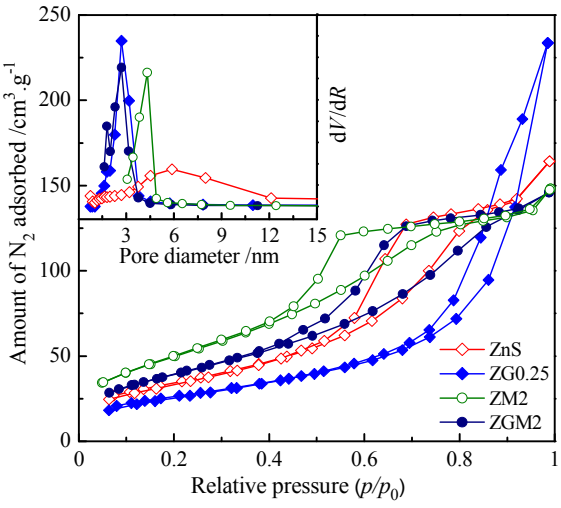

Fig. 5. Nitrogen adsorption–desorption isotherms of ZnS, ZG0.25, ZM2 and ZGM2. The inset indicates their pore size distribution curves.

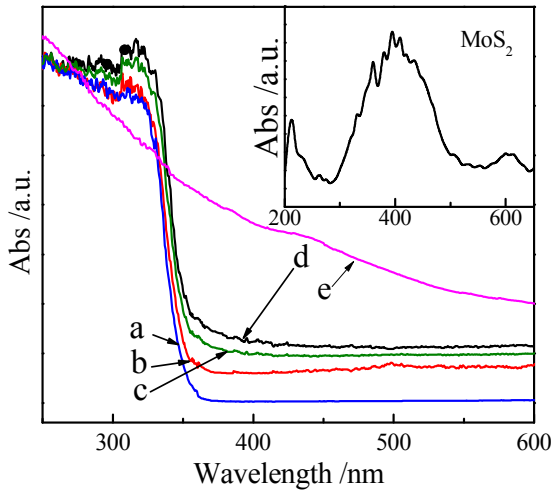

Fig. 6. UV-vis diffuse reflectance spectra of ZnS (a), ZG0.25 (b), ZM2 (c), ZGM2 (d) and RGO(e). The inset curve indicates the absorbance of MoS_2.

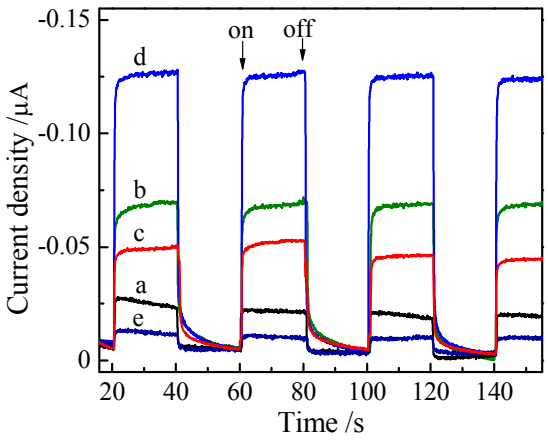

Fig. 7. Photocurrent-time curves of ZnS (a), ZG0.25 (b), ZM2 (c), ZGM2 (d) and MG (e).

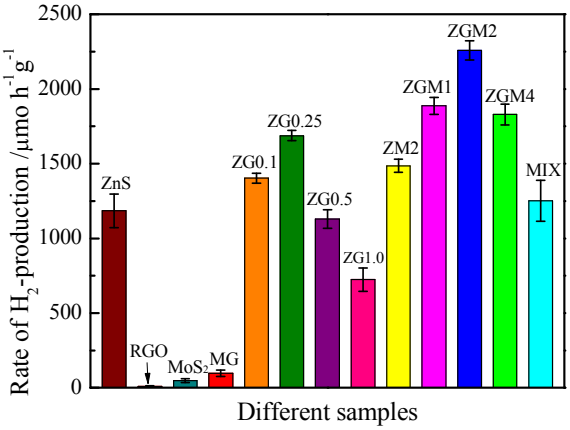

Fig. 8. Comparison of the H_2-production rates on different catalysts under the employed conditions of 100 mg catalyst, 100 mL aqueous solution containing 0.005 M Na_2S and 0.005 M Na_2SO_3, and 300-W xenon lamp irradiation, where MIX for the physical mixture of ZnS, graphene and MoS_2.

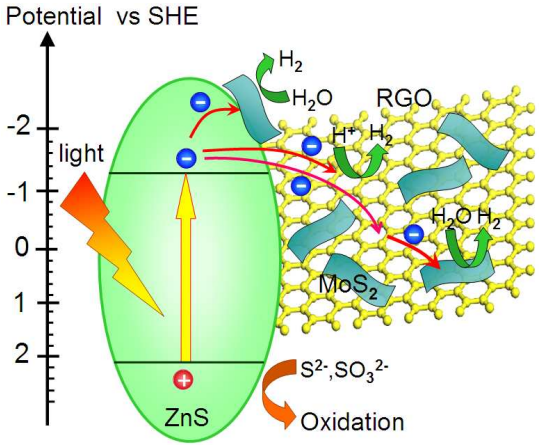

Fig. 9. Proposed mechanism for the enhanced electron transfer in ZGM composites.

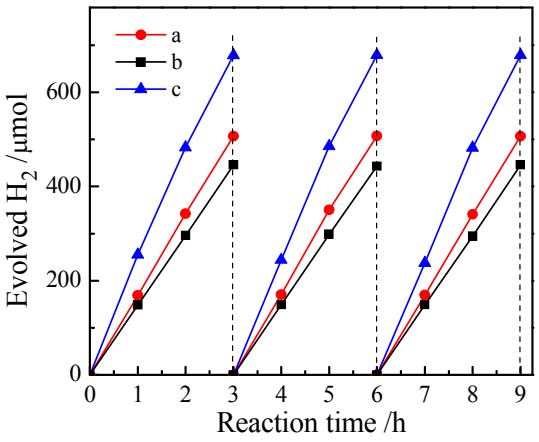

Fig. 10. Time-circle photocatalytic hydrogen evolution over ZG0.25 (a), ZM2 (b) and ZGM2 (c).

Enhanced photocatalytic H_2 evolution on ZnS loaded with graphene and MoS_2 nanosheets as cocatalysts

Bolin Zhu, Bizhou Lin*, Yi Zhou, Ping Sun, Qianru Yao, Yilin Chen and Bifen Gao

Contents Entry

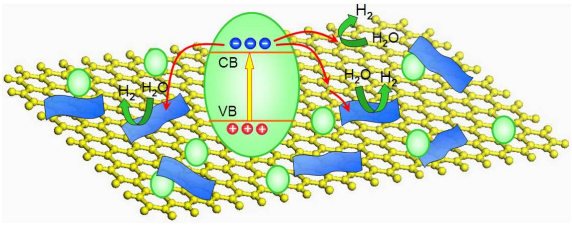

Efficient electron transfer for high photocatalytic H_2 evolution was obtained by immobilizing ZnS nanoparticles on the nanosheets of graphene and MoS_2.